

Chandra observations of the pulsar B1929+10 and its environment

Z. Misanovic, G. G. Pavlov, and G. P. Garmire

*Dept. of Astronomy and Astrophysics, The Pennsylvania State University, 525 Davey Lab.,
University Park, PA 16802*

ABSTRACT

We report on two *Chandra* observations of the 3-Myr-old pulsar B1929+10, which reveal a faint compact ($\sim 9'' \times 5''$) nebula elongated in the direction perpendicular to the pulsar's proper motion, two patchy wings, and a possible short ($\sim 3''$) jet emerging from the pulsar. In addition, we detect a tail extending up to at least $4'$ in the direction opposite to the pulsar's proper motion, aligned with the $\sim 15'$ -long tail detected in *ROSAT* and *XMM-Newton* observations. The overall morphology of the nebula suggests that the shocked pulsar wind is confined by the ram pressure due to the pulsar's supersonic speed. The shape of the compact nebula in the immediate vicinity of the pulsar seems to be consistent with the current MHD models. However, since these models do not account yet for the change of the flow velocity at larger distances from the pulsar, they are not able to constrain the extent of the long pulsar tail. The luminosity of the whole nebula as seen by *Chandra* is $L_{\text{PWN}} \sim 10^{30}$ ergs s^{-1} in the 0.3–8 keV band, for the distance of 361 pc. Using the *Chandra* and *XMM-Newton* data, we found that the pulsar spectrum is comprised of non-thermal (magnetospheric) and thermal components. The non-thermal component can be described by a power-law model with photon index $\Gamma \approx 1.7$ and luminosity $L_{\text{PSR}}^{\text{nonth}} \approx 1.7 \times 10^{30}$ ergs s^{-1} in the 0.3–10 keV band. The blackbody fit for the thermal component, which presumably emerges from hot polar caps, gives the temperature $kT \approx 0.3$ keV and projected emitting area $A_{\perp} \sim 3 \times 10^3$ m², corresponding to the bolometric luminosity $L_{\text{bol}} \sim (1\text{--}2) \times 10^{30}$ ergs s^{-1} .

Subject headings: pulsars: individual (PSR B1929+10) — stars: neutron — X-rays: stars

1. Introduction

Pulsar wind nebulae (PWNe), generated when the magnetized relativistic pulsar winds shock in the ambient medium, have been observed around ≈ 50 pulsars (see Kargaltsev & Pavlov

2008, for a recent review). The shocked pulsar winds produce synchrotron radiation from radio frequencies through γ -rays, revealing properties of the winds and the ambient medium.

The PWN morphology depends on the pulsar’s velocity, pressure, temperature, and magnetic field of the ambient medium, and the geometry of the wind outflow. For instance, the torus-jet PWN structures observed around young pulsars in supernova remnants (SNRs), such as the Crab and Vela PWNe (Weisskopf et al. 2000; Pavlov et al. 2003), are commonly interpreted as anisotropic outflows with equatorial and polar components confined by the pressure of the hot gas in the host SNR interiors, where the speed of sound exceeds the pulsar’s speed (Komissarov & Lyubarsky 2003; Del Zanna et al. 2004). When the pulsar is moving with a supersonic speed with respect to the ambient medium, bow-shock PWNe are formed (Bucciantini et al. 2005; Romanova et al. 2005), such as the PWNe around PSR J1747–2958 (the Mouse PWN; Gaensler et al. 2004) and PSR B1957–20 (Stappers et al. 2003). The pulsar’s supersonic speed causes the ram pressure to exceed the ambient pressure, so that the wind termination shock acquires a bullet-like shape (e.g. Bucciantini et al. 2005) and forms a PWN, sometimes with a long tail extending behind the pulsar. The pulsar’s speed becomes supersonic as it encounters a relatively cold interstellar medium (ISM), either after leaving the SNR in which it was born, or when the host SNR dissolves in the ISM background. These last stages of the SNR evolution occur after $\sim 10^5$ years.

The majority of middle-aged ($\sim 10^5$ – 10^6 yr) and old ($\gtrsim 10^6$ yr) pulsars are expected to move supersonically through the surrounding ISM, and as long as their winds are sufficiently strong, they are expected to produce observable bow-shock PWNe. Observations of these objects provide an opportunity to study bow-shock morphologies and probe pulsar winds and their surroundings at later stages of pulsar evolution.

Until now, only a handful of PWNe around middle-aged pulsars have been detected: e.g., PSR J0538+2817 (Romani & Ng 2003), PSR B0355+54 (McGowan et al. 2007), and Geminga (Caraveo et al. 2004; Pavlov et al. 2006) in X-rays, PSR B0906–49 at radio frequencies (Gaensler et al. 1998), and PSR B1951+32 in X-rays and $H\alpha$ (Moon et al. 2004). However, one of the first bow-shock PWN candidates was detected serendipitously around a much older pulsar, PSR B1929+10 (hereafter B1929). This is one of the nearest pulsars ($d = 361_{-8}^{+10}$ pc; Chatterjee et al. 2004), with a period $P = 226.5$ ms and period derivative $\dot{P} = 1.16 \times 10^{-16}$ s s $^{-1}$. Despite the large spindown age, $\tau \equiv P/2\dot{P} = 3.1$ Myr, its spindown power, $\dot{E} \equiv 4\pi^2 I \dot{P}/P^3 = 3.9 \times 10^{33}$ ergs s $^{-1}$ for the moment of inertia $I = 1 \times 10^{45}$ g cm 2 , is still relatively high. As the pulsar’s transverse velocity in the plane of the sky, $V_{\perp} = 177_{-5}^{+4}$ km s $^{-1}$ (Chatterjee et al. 2004), substantially exceeds the typical ISM sound speed, one can expect that the pulsar wind outflow forms a bow-shock PWN. An indication of such a PWN was first noticed by Wang et al. (1993), who detected a very long (~ 1.6 pc)

tail-like structure behind this pulsar in *ROSAT* data. The tail behind B1929 had been the longest extended structure associated with a compact Galactic object until the recent discovery of a 6-pc-long X-ray tail behind the middle-aged pulsar PSR J1509–5850, reported by Kargaltsev et al. (2006) and described in detail by Kargaltsev et al. (2008). Similar (albeit shorter) tails have been found behind a few other pulsars (Kargaltsev & Pavlov 2008) suggesting that such extended PWN morphologies might be ubiquitous.

The B1929 pulsar has been extensively observed in X-rays, in an attempt to study the magnetospheric and thermal components of its emission and compare them with the models for pulsar radiation. In particular, the thermal emission from polar caps heated by relativistic particles accelerated in the pulsar magnetosphere is predicted by the current pulsar models (e.g., Harding & Muslimov 2001, 2002), but a limited sample of the observed old pulsars suggests that the nonthermal magnetospheric emission with a power-law spectrum dominates at higher X-ray energies, $E \gtrsim 2$ keV, while the nature of radiation at lower energies has been a matter of debate (Becker et al. 2004, 2005; Zavlin & Pavlov 2004; Kargaltsev et al. 2006). Observations of B1929 with the *Einstein* (Helfand 1983), *ROSAT* (Yancopoulos et al. 1994; Becker & Trümper 1997), and *ASCA* (Wang & Halpern 1997; Kawai et al. 1998) observatories were not able to constrain the nature of the X-ray emission from the pulsar because its spectrum could be equally well described as thermal or non-thermal. The same result has been obtained by combining the available *ROSAT* and *ASCA* data by Słowikowska et al. (2005), who found that the spectrum of B1929 could be fitted either by a power-law or a two-temperature blackbody model.

Analyzing the images obtained in the 40 ks *ROSAT* PSPC observation, Wang et al. (1993) noticed an elongated structure extending approximately $10'$ behind B1929, almost aligned with the direction of its proper motion. Wang et al. (1993) have suggested that the detected tail is synchrotron radiation from the wind of B1929 confined by the ram pressure. The detection of this diffuse emission has also been reported by Yancopoulos et al. (1994) in the analysis of the same *ROSAT* PSPC data. Kawai et al. (1998) also claim detection of some diffuse emission in the vicinity of B1929 in the *ASCA* images, but the poor angular resolution of *ASCA* prevented a detailed analysis and did not allow to separate the contribution from background sources in the alleged PWN emission.

In a multi-wavelength study of B1929 (Becker et al. 2006), the tail-like structure extending up to more than 1 pc behind the pulsar has been observed by *XMM-Newton*, confirming the *ROSAT* finding. The spectral analysis suggests that this extended emission is nonthermal, likely produced by synchrotron radiation of the shocked pulsar wind. Becker et al. (2006) also report on an elongated faint diffuse radio emission found in the Effelsberg radio continuum survey data, whose brightness distribution roughly coincides with the X-ray

tail. These authors also conclude that the radiation of the B1929 pulsar is predominantly nonthermal (i.e., magnetospheric), with a rather soft power-law spectrum (photon index $\Gamma \approx 2.7$).

To understand the nature of the extended emission behind B1929 and prove that it is indeed a tail of a bow-shock PWN, the nebula in the immediate vicinity of the pulsar should be observed with an angular resolution much better than those of *ROSAT* PSPC (25") or *XMM-Newton* (15" half-energy width). Therefore, we conducted two *Chandra* observations of the B1929 pulsar and its surroundings. The first results, including the detection of a faint nebula in the immediate vicinity of B1929, have already been reported by Misanovic et al. (2006). In this paper we present a more detailed analysis of these observations.

2. Observations and results

We observed the field around B1929 with the Advanced CCD Imaging Spectrometer (ACIS) aboard *Chandra* (Table 1). Both observations were carried out in very faint mode on the ACIS-S3 chip, with the target imaged about 8" from the optical axis. The data were analyzed using the *Chandra* Interactive Analysis of Observations (CIAO) software (ver. 3.3.0.1; CALDB ver. 3.2.0 for observation 6657, and CALDB ver. 3.2.2 for observation 7230).

Table 1 also includes three archived *XMM-Newton* observations of B1929, which we analyzed in addition to the *Chandra* data, using SAS (ver. 7.1.0).

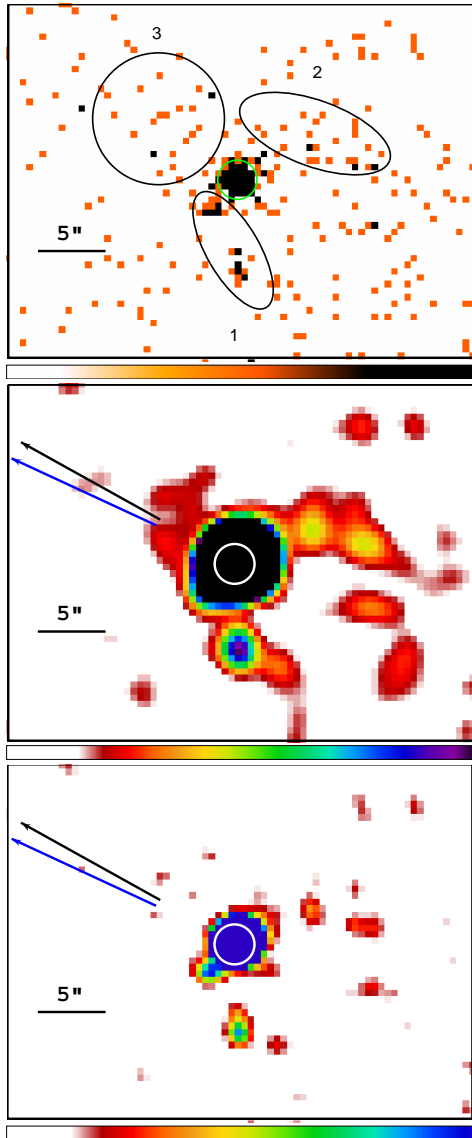


Fig. 1.— Images of the field around B1929 in the 0.3–8 keV band, combining the two ACIS-S3 observations. *Top*: Unsmoothed image (pixel size is $0.492''$). The circular and elliptical regions mark the smallest structures detected around the pulsar at $\geq 3\sigma$ levels in at least one of the observations (see Table 2). *Middle*: The same image smoothed using a Gaussian of FWHM $1''$. The blue arrow shows the direction of the measured pulsar’s proper motion (Chatterjee et al. 2004), while the black arrow indicates the proper motion corrected for the Galactic rotation and solar peculiar velocity (see text for details). *Bottom*: In this image the pulsar contribution is subtracted (see text for details) and smoothing with a Gaussian of FWHM $0.5''$ is applied. The brightness scales in the middle and bottom panels are selected to emphasize different components of the extended emission in the vicinity of B1929. The intensity scale is linear, with a range of 0 to 1.8 cts/pixel in the top panel, and 0 to 0.9 cts/pixel (middle and bottom). The position of the pulsar is indicated by a $1.5''$ circle in all panels.

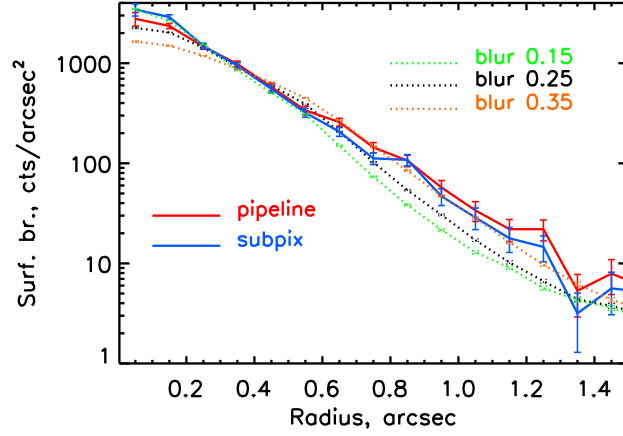


Fig. 2.— Radial profiles of the combined pipeline-processed and subpixelized data (solid lines), and MARX-simulated data (dotted lines) for various blurring parameters (see text). The counts are measured in annular regions centered at the pulsar’s position.

2.1. X-ray imaging

We first produced new level-2 event files with the pipeline pixel randomization disabled and then applied the method by Mori et al. (2001) and Tsunemi et al. (2001), which allows one to reach a subpixel spatial resolution. To minimize the background contribution, we chose the energy band of 0.3–8 keV.

The only relatively bright source on the S3 chip is the B1929 pulsar, centered at R.A. = $19^{\text{h}}32^{\text{m}}13.999^{\text{s}}$, decl. = $10^{\circ}59'32.64''$, and R.A. = $19^{\text{h}}32^{\text{m}}14.000^{\text{s}}$, decl. = $10^{\circ}59'32.85''$ (J2000) in the first and second observation, respectively (the centroiding 1σ uncertainty is $0.02''$ for each coordinate, as determined by the CIAO procedure `CELLDETECT`). The offsets of these positions from the radio positions of the pulsar extrapolated to the epochs of the two observations ($0.17''$ and $0.14''$ in R.A., $-0.04''$ and $0.16''$ in decl., respectively) are smaller than the error in the absolute *Chandra* astrometry, $0.45''$ at the 90% confidence level for on-axis observations on the S3 chip¹.

2.1.1. Combined ACIS image.

Although both images show some extended emission in the immediate vicinity of the pulsar, its surface brightness is very low. Therefore, to increase the signal-to-noise ratio, we have to combine the two ACIS observations. To align the images, we reprojected the event files to a common position, corrected the aspect solution of the second observation for the pulsar’s positional difference of $0.02''$ in R.A. and $0.21''$ in decl., and added the two images.

A nebula surrounding the pulsar is clearly seen in the unsmoothed and smoothed images shown in the top and middle panels of Figure 1. To separate this extended emission from the pulsar, we simulated the ACIS-S3 point source observations using the *Chandra* data simulator MARX². We produced simulated images of a point source at the same position on the detector, and with the same X-ray flux and spectral shape as those of the observed pulsar, running MARX for an effective exposure 100 times longer than the actual observations to reduce statistical errors. The simulated images were then scaled to the actual exposure times, combined, and compared with the data, both pipeline-processed and those with subpixel resolution.

¹See §5.4 and Fig. 5.4 in the *Chandra* Proposers’ Observatory Guide, ver. 10, at <http://asc.harvard.edu/proposer/POG>.

²See <http://space.mit.edu/CXC/MARX/>

The width of the simulated point spread function (PSF) depends on the value of the MARX parameter Dither Blur, which is a combination of the aspect reconstruction error, ACIS pixelization, and pipeline pixel randomization. According to the MARX manual³, appropriate values of this parameter are about $0.35''$ if the pixel randomization is applied and $0.20''$ – $0.25''$ if it is switched off, but the best values of this parameter may vary from observation to observation.

We found that for the default Dither Blur = $0.35''$, the simulated PSF is significantly *broader* than the core of the observed B1929 image, not only for the sharper image with subpixel resolution but also for the pipeline-processed one (see Fig. 2). We repeated the simulation for a number of smaller Dither Blur values and found that the PSF core of the simulated data with Dither Blur reduced to $0''.15$ matched well to the data with subpixel resolution, while a simulation with Dither Blur = $0.25''$ is close to the pipeline-processed data. In both cases, the shape of the simulated PSF matched well to the observed one only up to $\approx 0.6''$ from the center, indicating the contribution of extended emission at larger distances from the pulsar. Using the excess of the data counts with respect to the simulation in the $0.5''$ – $1.5''$ annulus, we estimate the signal-to-noise ratio of the PWN to be $\gtrsim 20$. For comparison, we also simulated the ACIS-S observation of the central compact source of the Cas A SNR (ObsID 6690) and found no indication of an extended emission around this point source.

The PWN image in the vicinity of B1929, obtained by subtracting the simulated data with Dither Blur = $0.15''$ from the subpixel resolution image and slight smoothing with a Gaussian of $0.5''$ FWHM, is shown in the bottom panel of Figure 1. The image reveals a compact, $\sim 9'' \times 5''$, emission elongated in the direction perpendicular to the pulsar’s proper motion, two faint wings extending in the direction opposite to the pulsar’s motion and seen up to $\sim 11''$ from the pulsar, and a hint of a short, $\sim 3''$, linear structure immediately behind the pulsar.

³See also http://www.astro.psu.edu/xray/docs/TARA/ae_users_guide/node16.html for a more detailed discussion.

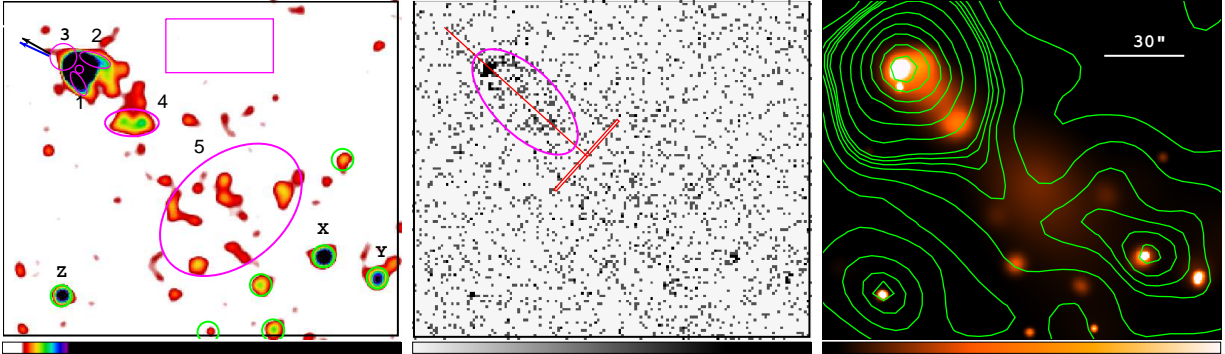


Fig. 3.— *Left:* ACIS-S3 image of B1929 and its environment produced by combining observations 6657 and 7230, in the 0.3–8 keV band. The unbinned image is smoothed using a Gaussian of FWHM $2''$. The elliptical regions mark the smallest structures detected around B1929 (see Table 2 and Fig. 1). The pulsar’s position is marked by a $1.5''$ circle, while the $40'' \times 20''$ box shows the region used for the background evaluation. The arrows indicate the direction of the pulsar’s proper motion (as in Fig. 1). The green circles enclose the optical/infrared sources in the field of view. The X marks the X-ray source found with CELLDETECT in the combined image, while Y and Z mark other possible X-ray point sources that might be just below the detection threshold. *Middle:* Unsmoothed combined image showing the same region. The image is binned by a factor of two. The ellipse shows the region of enhanced emission, in which the diffuse emission is detected at a $\sim 10\sigma$ level in the combined image. The red box and the line mark the size of the rectangular region and the direction in which the region is moved to produce the linear profile shown in Fig. 4. *Right:* The same unbinned image smoothed using an adaptive Gaussian kernel with the size self-adjusting to show the structures with the signal-to-noise ratio in the range 2.2 to 4. The overlaid contours correspond to the combined *XMM-Newton* observations. The contour levels are the same as in Fig. 5. The intensity scale is linear in all images, with a range of 0 to 0.2 cts/pixel in the left and right panels and 0 to 1.8 cts/pixel (middle).

After confirming that there is a PWN in the immediate vicinity of B1929, we proceeded by searching for the nebular emission farther from the pulsar. Figure 3 shows a $2.5' \times 2.5'$ image combining the two *Chandra* observations. The image on the left is smoothed using a fixed-size Gaussian of $2''$ FWHM, while the right panel shows a heavily smoothed image using an adaptive kernel with an adjustable size to show the structures with the signal-to-noise ratio in the range 2.2 to 4. The middle panel shows the combined unsmoothed data binned by a factor of two. The images show several regions of extended emission: a bow-shock-shaped extended emission with the Southern Wing (region 1) and Northern Wing (region 2), some faint emission in front of the pulsar (region 3 or the Front), faint diffuse emission elongated in the direction opposite to the direction of the pulsar’s projected velocity, with an enhancement at the distance of $\approx 30''$ (region 4 or the Inner Blob). A more extended but fainter region 5 (Outer Blob) is seen farther behind the pulsar, at a distance of approximately $1.5' - 2'$. Regions 1 through 3 are also shown in the top panel of Figure 1, while the numbers of counts in the regions are given in Table 2.

Although these structures (regions 1 to 5) were detected at a level of at least 3σ in one or both individual observations, the small number of detected counts prevented the detailed spectral analysis. Therefore, we selected a larger region of the extended emission to study the spectral properties of the PWN (§2.3.2). The region is marked by the ellipse (semi-axes $12''$ and $25''$) in the middle panel of Figure 3, detected at a level of at least 5σ in each observation.

The blue arrows in Figures 1 and 3 indicate the direction of the pulsar’s proper motion ($\mu_\alpha = 94.09 \pm 0.11 \text{ mas yr}^{-1}$, $\mu_\delta = 42.99 \pm 0.16 \text{ mas yr}^{-1}$) as measured by Chatterjee et al. (2004) with respect to extragalactic reference radio sources. To determine the proper motion with respect to the local ISM, we corrected the measured proper motion for the effects of Galaxy rotation and the Sun’s peculiar motion with respect to the local standard of rest (LSR). Following the procedure by Johnson & Soderblom (1987), and adopting the value for the Sun’s peculiar velocity from Boesgaard & Tripicco (1986) and Oort constants from Binney & Tremaine (1987), we obtained the corrected proper motion $\mu_\alpha = 91.6 \pm 0.2 \text{ mas yr}^{-1}$, $\mu_\delta = 49.1 \pm 0.2 \text{ mas yr}^{-1}$, shown by the black arrows in Figures 1 and 3. The total proper motion, $\mu = 104.0 \pm 0.3 \text{ mas yr}^{-1}$, corresponds to the transverse velocity $v_\perp = 178 \pm 8 \text{ km s}^{-1}$. Its direction (position angle $61.7^\circ \pm 0.1^\circ$, counted East of North) seems to be better aligned with the extended tail of diffuse emission, which further supports the PWN interpretation of the detected X-ray emission around this pulsar.

Since the observed diffuse emission might be partly due to unresolved point X-ray sources in the field of view (e.g., stars or background AGNs), we examined available optical, near-infrared, and radio data of the region around B1929. We found several sources (marked with

the green circles in Fig. 3, *left*) in the USNO-B2 (Monet et al. 2003) and 2MASS (Cutri et al. 2003) catalogs, which coincide with the regions resembling faint point-like objects in our smoothed images. Although these possible sources are very faint in the *Chandra* images (only one of these sources, marked with an X, was detected by the CIAO tool CELLDETECT above the source threshold of 3, while Y and Z mark other two possible X-ray point sources that might be just below the detection threshold), they might contribute to the observed extended emission. It is clear, however, that most of the detected tail-like structure is indeed diffuse emission associated with the pulsar.

Figure 4 shows the brightness distribution along the tail, which further demonstrates the excess emission over the background in front of the pulsar, and also in the direction approximately opposite to the projected pulsar’s velocity. The photons were collected from $1'' \times 35''$ rectangular regions (see Fig. 3) along the tail, and also from the background regions of the same area on both sides of the tail in the unsmoothed combined *Chandra* image. We show only the brightest part of the tail, up to $\sim 40''$ from the pulsar, because the extended emission farther away is too faint and cannot be distinguished from the background using such small collecting regions, but it is much better seen in the smoothed image.

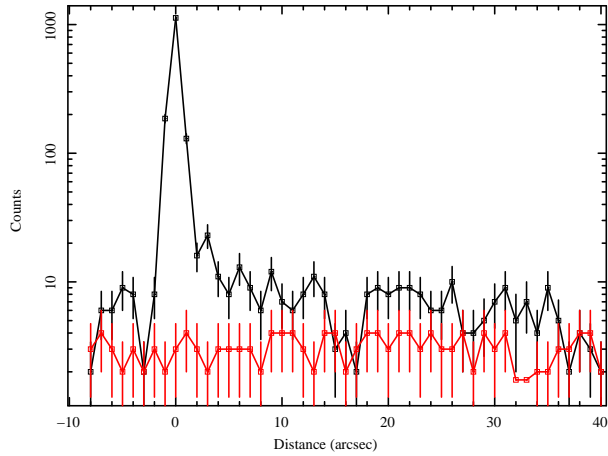


Fig. 4.— X-ray linear brightness profile along the direction of the pulsar’s tail. The black data points were obtained by counting the photons in the $1'' \times 35''$ rectangular regions (see Fig. 3). The pulsar moves towards the negative values on the X-axis. The red data points show the X-ray profile of the background emission, evaluated in the rectangular regions of the same size on both sides of the tail emission.

To look for extended emission at even larger distances from the pulsar and compare it with the $10' - 15'$ tail detected by Becker et al. (2006), we produced heavily binned images shown in Figure 5. Although the smaller ACIS-S field of view and the relatively short *Chandra* exposure do not allow us to detect the full extent of the faint diffuse emission observed by *XMM-Newton*, at least some parts of the B1929 long tail are seen up to $\approx 4'$ from the pulsar in the combined ACIS-S3 image. The long tail extends from the compact PWN resolved in the *Chandra* images in the same direction as the emission detected in *XMM-Newton* data.

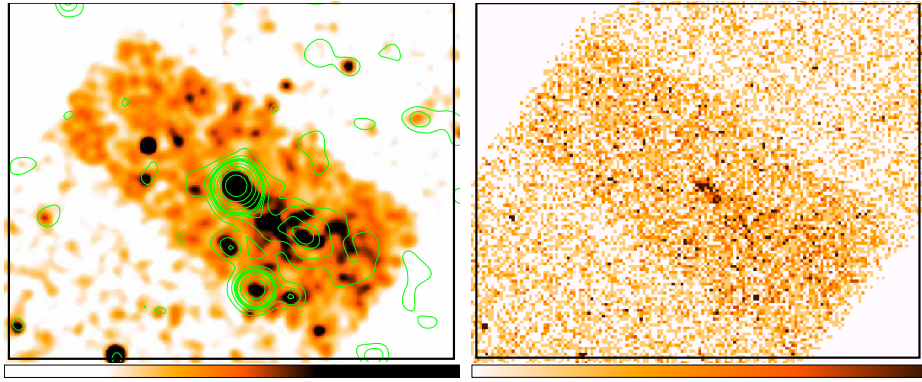


Fig. 5.— $10' \times 8'$ ACIS-S3 field around B1929. The image on the left is produced from the combined event file, binned by a factor of 4 and then smoothed by a Gaussian of FWHM $6''$. The contours, at levels 0.08, 0.1, 0.12, 0.13, 0.14, 0.15, 0.2, 0.3, 0.5, 0.9, 2 and 5 counts pixel^{-1} , correspond to the three combined *XMM-Newton* observations (MOS1 and MOS2 data, pixel size $1.1''$). The right panel shows the same image, which is binned by a factor of 8 but not smoothed. To minimize the background, both images include only the 0.5–7 keV energy range. The intensity scale is linear, with ranges of 0 to $0.8 \text{ counts pixel}^{-1}$ (left) and 0 to $6 \text{ counts pixel}^{-1}$ (right).

2.1.2. Individual observations and variability

Since some PWNe show significant temporal variations on time-scales of months (e.g., the Crab and Vela PWNe, Hester et al. 2002; Pavlov et al. 2003), we have examined the individual ACIS-S observations, which are separated by $\simeq 6$ months, in search for variability of the PWN of B1929. Figure 6 shows the images of the individual *Chandra* observations of B1929 and its PWN. Similarly to the combined data, the images on the left were smoothed using a Gaussian of FWHM $2''$, while on the right we show the same images adaptively smoothed to reveal structures with the signal-to-noise ratio in the range 2.2 to 4. The bright features seen in the combined image (Fig. 3) are also visible in these individual images, but their apparent brightness seem to show a substantial difference between the observations. For example, the Inner Blob (region 4), clearly detected in the observation 6657 (December 2005), is not visible in the image of the observation 7230 (May 2006), while the Outer Blob (region 5) appears fainter and slightly smaller in the second observation. In addition, the Southern Wing and the emission in front of the pulsar (region 3) are slightly brighter in the observation 6657, while the Northern Wing is brighter in the second observation.

To quantify this apparent variability, we measured the total background-subtracted counts detected in each of the extended regions in the unsmoothed images of both data sets, and calculated the corresponding surface brightness (listed in Table 2). The background emission was determined using the rectangular region with an area of 784 arcsec^2 shown in Figure 3 (left), from which we measured $(3.3 \pm 0.4) \times 10^{-6} \text{ cts s}^{-1} \text{ arcsec}^{-2}$ and $(2.2 \pm 0.4) \times 10^{-6} \text{ cts s}^{-1} \text{ arcsec}^{-2}$ in the observations 6657 and 7230, respectively.

As shown in Table 2, the surface brightness of the five extended regions is found to change by a factor of two (e.g. region 1) or even four (region 3). However, due to the large statistical errors, the variability could only be detected at a level of up to $\approx 2.5\sigma$ (region 5). Deeper observations would be needed to further examine possible variability of the nebula associated with this old pulsar. We also note that the variation of the pulsar count rates between the two *Chandra* observations was found to be within the statistical uncertainty (see § 2.3.1).

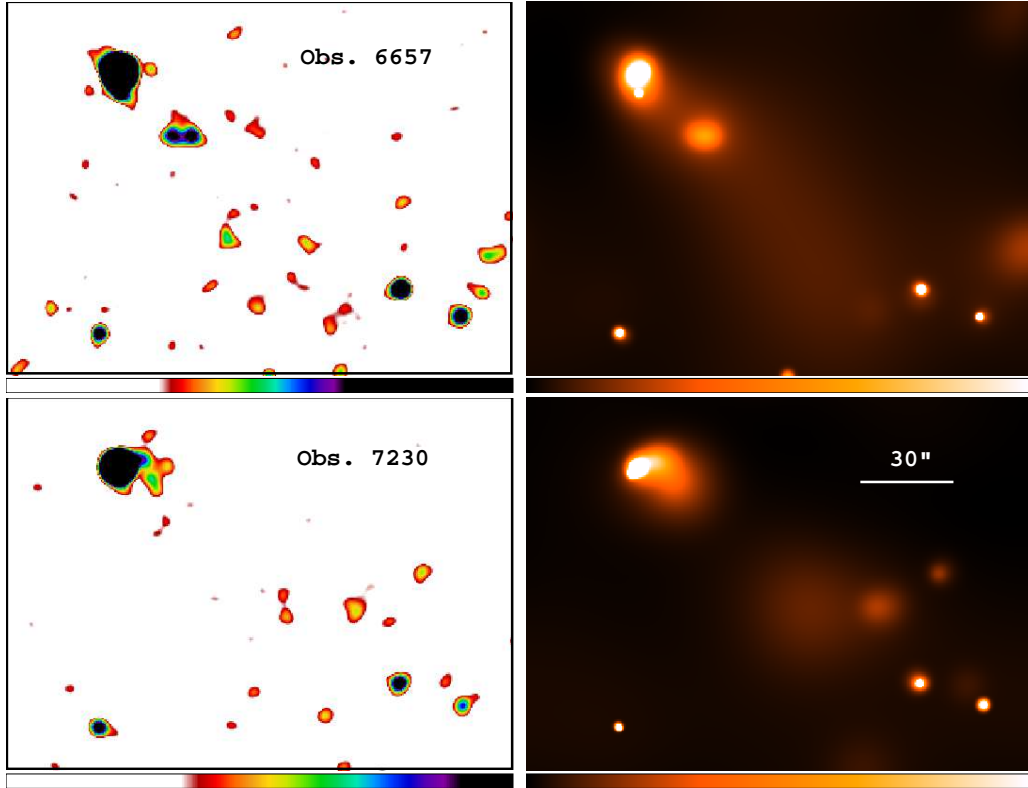


Fig. 6.— *Left:* 0.3-8 keV images of the first (*top*) and second (*bottom*) ACIS-S3 observations, smoothed using a Gaussian of FWHM 2". *Right:* The same images adaptively smoothed to show the structures with the signal-to-noise ratio in the range 2.2 to 4. The intensity scale is linear with a range of 0 to 0.2 cts/pixel in all panels.

2.2. Connection with the *XMM-Newton* data

To examine the connection between the *Chandra* and *XMM-Newton* data on the PWN, we produced combined MOS1 and MOS2⁴ broad-band images for each of the three available *XMM-Newton* observations of the B1929 field listed in Table 1 (see Becker et al. 2006, for more detail about the *XMM-Newton* data and for the combined image of all three observations).

The smoothed images are shown in Figure 7, overlaid with the structures detected in the ACIS-S observations. Since the MOS PSF is much broader than that of ACIS, the compact PWN (regions 1–3 in Figs. 1 and 3) and the beginning of the PWN tail (region 4) cannot be resolved from the pulsar. However, at least in the first two *XMM-Newton* observations we clearly see the local brightening in the PWN tail $\approx 2'$ from the pulsar, approximately coinciding with the Outer Blob (region 5) detected in the *Chandra* data. From the three unsmoothed MOS1 images, we calculated an average background-subtracted count rate of 1.5 ± 0.3 counts ks⁻¹ in the Outer Blob. With account for different ACIS-S and MOS1 responses, this count rate is consistent with that measured in the combined *Chandra* data in the same region (see Table 2).

⁴The PN observations were taken in the small-window mode and have high background.

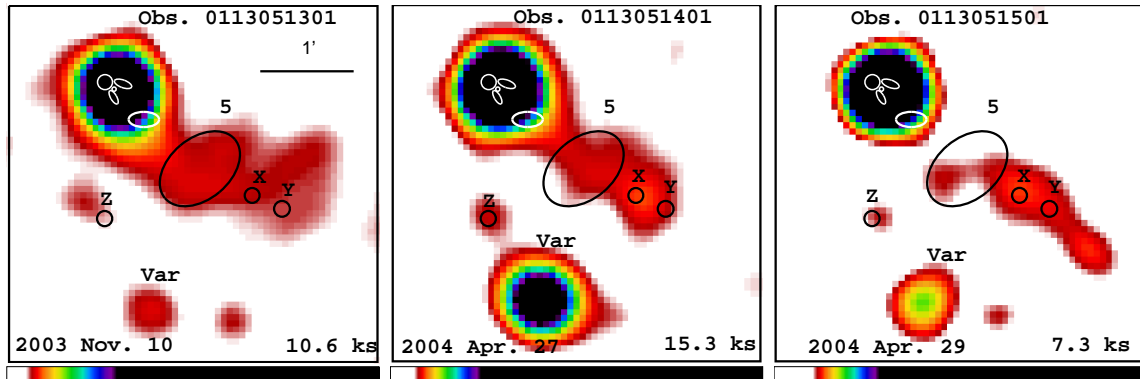


Fig. 7.— Combined MOS1+MOS2 images of B1929 and its surroundings in the three *XMM-Newton* observations. Broad-band (0.3–10 keV) images were smoothed using a Gaussian of FWHM $6''$. The five regions of enhanced emission and possible pointlike sources X, Y and Z detected in the ACIS-S observations are shown (see left panel of Fig. 3 and Table 2). The bright source (Var) $\sim 2.5'$ south from the pulsar exhibits strong variability, also clearly visible in the unsmoothed MOS images. The intensity scale is linear, with a range of 0 to 6 counts per pixel in all panels.

Since our *Chandra* data indicate possible variability of the PWN, we examined the *XMM-Newton* data for brightness variations in the extended emission. From the number of the background-subtracted counts in the Outer Blob, we determined the averaged MOS1 count rates of 1.7 ± 0.5 , 1.6 ± 0.5 , and 1.3 ± 0.5 counts ks^{-1} in observations 0113051301, 0113051401 and 0113051501, respectively. Thus, although the Outer Blob changes its surface brightness by a factor of 2 at a 2.5σ level in our ACIS-S data, the surface brightness of the same region in the MOS1 data, separated by approximately the same period of ~ 5 months as the two *Chandra* pointings, does not show a significant brightness change.

Figure 7 suggests that the region southwest of the Outer Blob might be variable. However, in the ACIS image we see no diffuse emission in this area, but there are two faint pointlike sources, X and Y (see Figs. 3 and 7). Hence, the apparent variability of this region could be due to the variability of these two sources, which could not be resolved in the *XMM-Newton* observations. Thus, although the *Chandra* observations hint that the tail of B1929 might be variable on time-scales of several months, longer high-resolution observations are required to firmly establish this variability.

Interestingly, the *XMM-Newton* images show a highly variable source (Var) $\sim 2.5'$ south of the pulsar. It was almost as bright as the pulsar in the 2004 April 27 observation, while it is barely visible in the 2003 November 10 image. The source was at the edge of the S3 chip in the first *Chandra* observation and barely detectable. However, it completely disappeared in the second observation, although its position was within the field of view. As it is apparently a point source, strongly detached from the other PWN structures, we conclude that it is unrelated to the B1929 PWN.

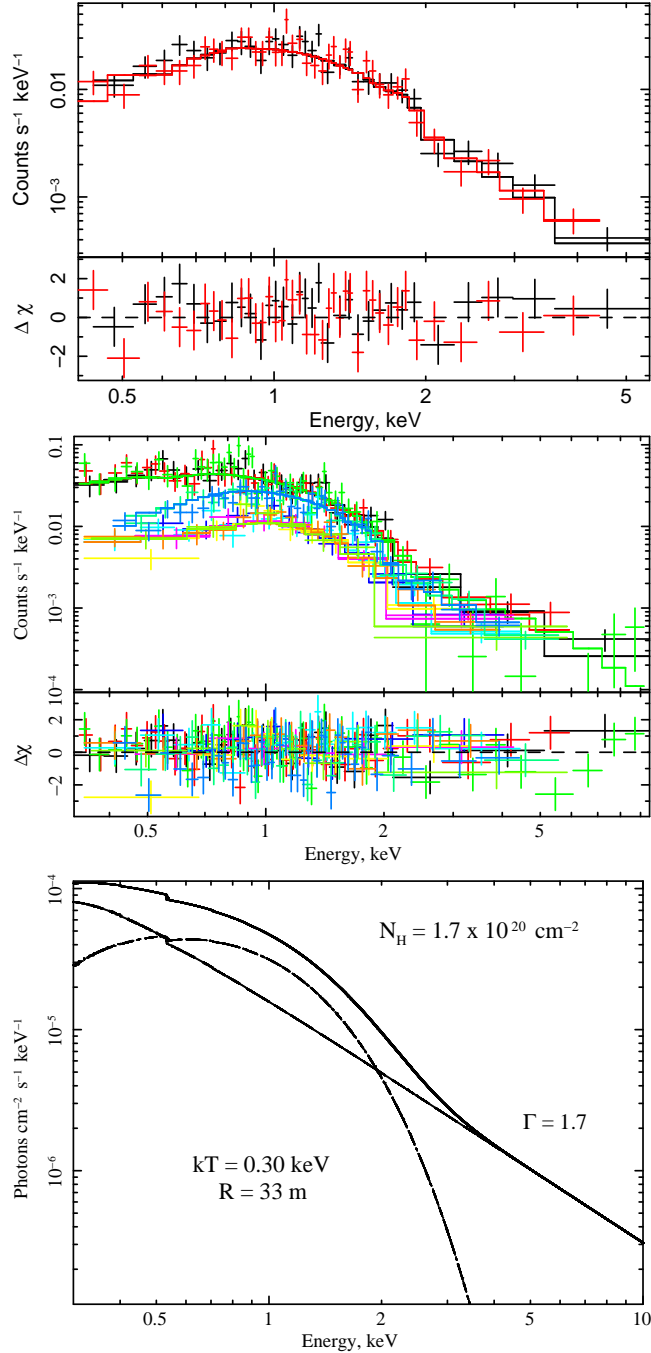


Fig. 8.— *Top*: Spectra of B1929 extracted from the *Chandra* observations 6657 (black) and 7230 (red) and the best-fit absorbed PL model. The model parameters are given in Table 3. *Middle*: PN, MOS1 and MOS2 spectra of B1929 extracted from the three *XMM-Newton* observations (PN: black, red, green; MOS1: blue, cyan, magenta; MOS2: yellow, orange, lime-green; in the observations 0113051301, 0113051401 and 0113051501, respectively), and fitted simultaneously with the *Chandra* data (Obs. 6657: dark-green; Obs. 7230: dark-blue) using the absorbed PL+BB model. The model parameters are given in Table 3. *Bottom*: Photon spectrum for the best-fit absorbed BB+PL model and its components. The unabsorbed luminosity of the BB component, $\approx 1.2 \times 10^{30} \text{ ergs s}^{-1}$, is estimated to be $\sim 45\%$ of the total luminosity, $\approx 2.6 \times 10^{30} \text{ ergs s}^{-1}$, in the 0.3–8 keV band.

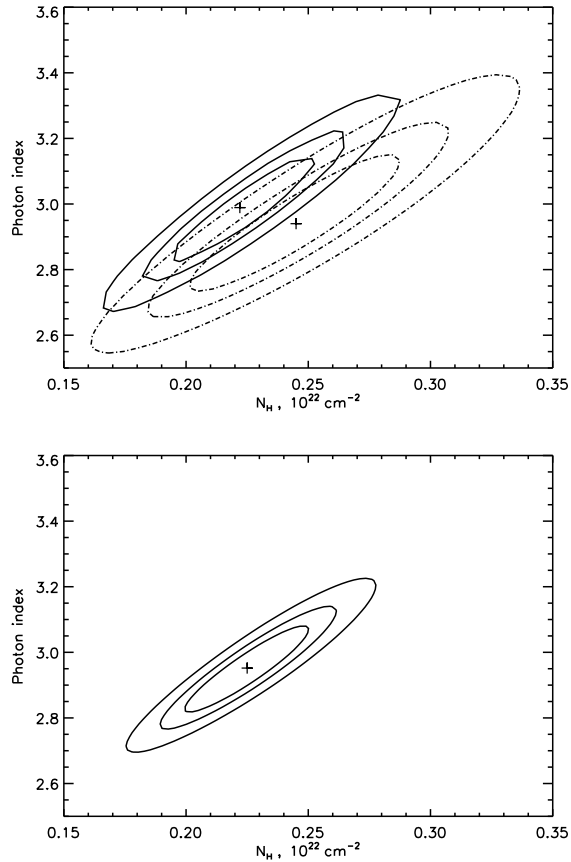


Fig. 9.— *Top*: 68%, 90%, and 99% confidence contours for the *Chandra* ACIS and *XMM-Newton* EPIC spectra of B1929 (dashed and solid lines, respectively), computed for two interesting parameters for the PL model. *Bottom*: 68%, 90%, and 99% confidence contours for the *Chandra* and *XMM-Newton* observations fitted simultaneously with the PL model.

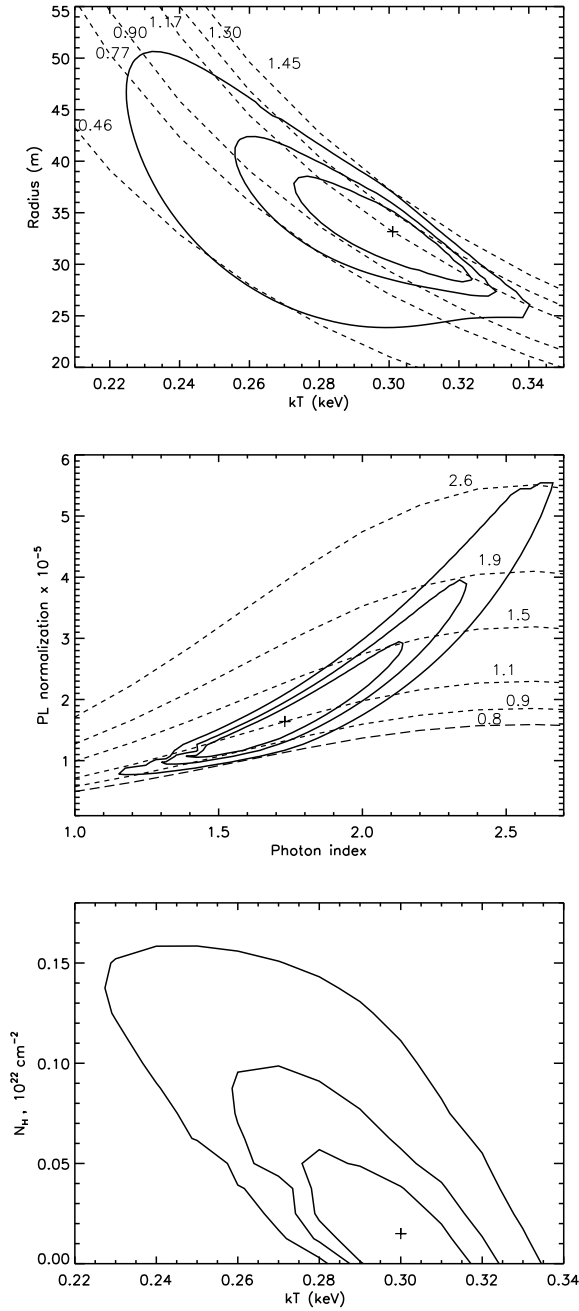


Fig. 10.— 68%, 90%, and 99% confidence contours for various parameter pairs for the PL+BB fit to the spectrum of B1929. The confidence levels correspond to two interesting parameters. The *Chandra* ACIS-S and *XMM-Newton* spectra are fitted simultaneously with all parameters allowed to vary. The top panel shows the lines of constant bolometric luminosity of an equivalent sphere (see § 3.2) in units of $10^{30} \text{ ergs s}^{-1}$ for the BB component, while the middle panel shows the lines of constant unabsorbed flux in units of $10^{-13} \text{ ergs cm}^{-2} \text{ s}^{-1}$ for the PL component.

2.3. Spectral analysis

2.3.1. The pulsar

The spectral *Chandra* data reduction was done by applying the standard procedures in CIAO. From a circular region with a radius of $1.6''$ (or 3.3 pixels) centered on the pulsar, we extracted 645 and 690 counts from the first and second observation, respectively. Four circular background regions, each with a radius of $5''$, were selected in the vicinity of the pulsar and then combined and used for the background subtraction. The background contribution in the source aperture is negligibly small (~ 1 count in each of the observations), but the aperture may include a small number of photons emerging from the compact nebula. Using the radial profiles in Figure 2, we estimated the PWN contribution to be around 2%–3%; hence it does not influence the results of the spectral fitting significantly. We grouped the extracted counts in a minimum of 15 and 17 counts per energy bin for the spectral analysis. The response matrices (rmf) were calculated using the CIAO task MKACISRMF, and the spectral analysis was performed using XSPEC (ver. 11.3.2).

Since we did not find statistically significant changes between the two *Chandra* observations, we fit both data sets simultaneously. The absorbed power-law (PL) model yielded a very good fit (Table 3; Fig. 8, top), albeit with surprisingly large best-fit hydrogen column density, $N_{\text{H}} \approx 2.5 \times 10^{21} \text{ cm}^{-2}$, and photon index, $\Gamma \approx 2.9$. On the contrary, we were not able to produce a statistically acceptable fit with the absorbed blackbody (BB) model as the discrepancy between the best-fit model and the data was large below 0.7 keV and particularly above 2 keV, resulting in $\chi^2_{\nu} = 1.86$ (vs. $\chi^2_{\nu} = 0.91$ for the PL fit) for 71 d.o.f.

The pulsar models predict that a thermal component from heated polar caps, and perhaps from the whole NS surface, may be detectable, making the main contribution at lower photon energies. Therefore, we attempted to fit the *Chandra* spectra with the PL+BB model. The addition of the BB component, with the best-fit temperature $kT \approx 0.3$ keV and emitting area $A \sim 4 \times 10^3 \text{ m}^2$, resulted in a substantially smaller hydrogen column density, $N_{\text{H}} < 1.4 \times 10^{21} \text{ cm}^{-2}$, and a softer PL spectrum, $\Gamma \approx 1.8$ (see Table 3), but the probability that the BB component is required by the data was only 69.5%, according to the F-test. We also tested the BB+BB model, but it yielded either statistically unacceptable fits or unphysical fitting parameters (e.g., $kT \sim 100$ keV, or an extremely low absorption column).

To compare the *Chandra* ACIS spectra with those obtained with the *XMM-Newton* EPIC detector, we extracted and fitted the pulsar spectra from the three *XMM-Newton* observations. The source counts were extracted from a circular region with a radius of $13''$ centered on the pulsar, while a $38''$ -radius circular region northwest of the pulsar was used for the background subtraction. We collected a total of 450 (with 96.8% of the source

contribution), 658 (94.8%) and 805 (75.3%) counts in the PN (small-window mode) observations 0113051301, 0113051401, and 0113051501, respectively. In addition, we extracted 172 (98.0%), 282 (97.3%), and 110 counts from the MOS1, and 153 (97.3%), 276 (98.0%), and 121 (96.8%) from the MOS2 observations, with MOS cameras operated in the large window mode. The EPIC response matrices and ancillary files were calculated using the SAS tasks RMFGEN and ARFGEN. From the number of the PWN counts detected with ACIS in an aperture of $13''$, we estimate that the contribution from the nebula in the EPIC spectra is about 5%.

Fitting all the 9 *XMM-Newton* data sets (PN, MOS1 and MOS2 in the three observations) simultaneously, we found that the PL model produced a statistically acceptable fit, with the model parameters consistent with those obtained from the *Chandra* data (Fig. 9)⁵. Adding the BB component to the spectral model resulted in about the same fitting parameters as for the *Chandra* data alone (Table 3), but improved the fit more significantly (94.8%, according to the F-test).

Finally, we fit the *Chandra* and *XMM-Newton* data simultaneously, first with the PL model. Because of the larger PWN contribution in the *XMM-Newton* data, we first linked all the model parameters except for the PL normalization. However, since we found that the difference between the PL normalizations in the *Chandra* and *XMM-Newton* spectra was within the statistical errors, we finally linked all the model parameters. As expected, we obtained the PL parameters similar to those obtained from the separate fits to the *Chandra* and *XMM-Newton* data, but with smaller uncertainties (Fig. 9, bottom).

Fitting the combined data with the PL+BB model, we found that the addition of the BB component provided a very significant improvement of the fit (99.98%, according to the F-test). The best PL+BB fit is shown in Figure 8, the fitting parameters are given in Table 3, and the confidence contours for various model parameters are presented in Figure 10. We note that the hydrogen column density, $N_{\text{H}} < 4 \times 10^{20} \text{ cm}^{-2}$, is significantly lower in the PL+BB fit and consistent with the value estimated from the pulsar’s dispersion measure, while the slope of the PL components, $\Gamma \approx 1.7$, is similar to those found in many other pulsars (see § 3.2 for further discussion).

⁵We should mention that our PL fitting parameters differ significantly from those obtained by Becker et al. (2006) from fitting the combined *XMM-Newton* EPIC and *ROSAT* PSPC data (they do not provide model parameters from fitting the *XMM-Newton* data separately). For instance, these authors obtained a lower hydrogen column density, $N_{\text{H}} = (1.6 \pm 0.2) \times 10^{21} \text{ cm}^{-2}$, and a smaller photon index, $\Gamma = 2.72_{-0.09}^{+0.12}$. We believe that the discrepancy is caused by systematic errors due to poor cross-calibration of the PSPC and EPIC detectors.

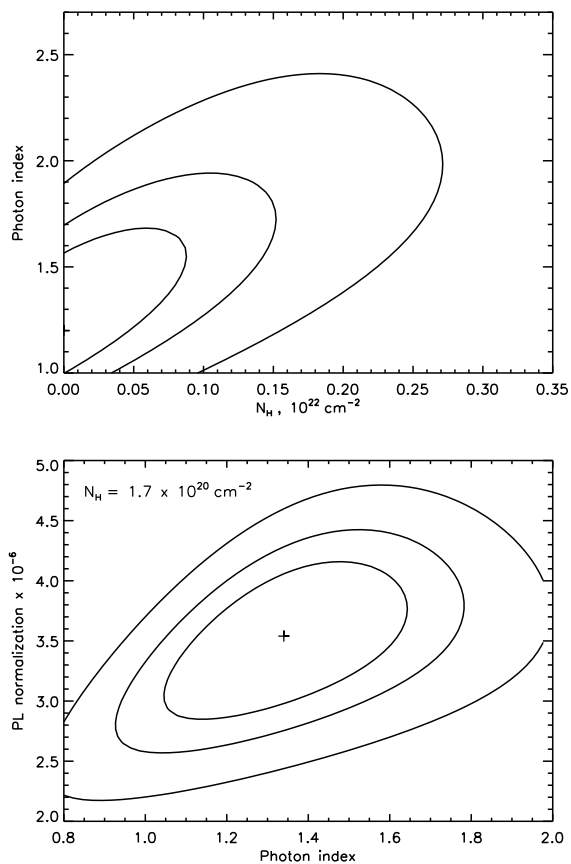


Fig. 11.— *Top*: 68%, 90%, and 99% confidence contours in the $N_{\text{H}} - \Gamma$ plane of the PL model for the PWN spectral data (the elliptical region in Fig. 3). *Bottom*: 68%, 90%, and 99% confidence contours in the Γ -Normalization plane of the PL model with the absorption column fixed to the best-fit value obtained from the spectrum of the pulsar.

2.3.2. The nebula

As the detected PWN is very faint, we have to choose a sufficiently large extraction region to measure its spectrum. The large-scale PWN appears to consist of a smaller, slightly brighter part up to $30''$ behind the pulsar (marked by the ellipse in the middle panel of Figure 3), and a fainter emission farther down, up to a distance of $\sim 2'$. From the brighter part of the nebula region (the ellipse) we collected 138 and 136 counts (64% and 63% of which are from the nebula) in the first and second observation, respectively.

To constrain the model parameters, we fit the spectra from the two observations simultaneously, with the absorbed PL model. The fit yielded a PL slope $\Gamma=1.0\text{--}1.7$ at a 90% confidence level (Fig. 11, top) and an absorption column $N_{\text{H}} = 0.0 - 0.9 \times 10^{21} \text{ cm}^{-2}$ (90% confidence). We also fitted the PWN spectra with the absorption column fixed to the best-fit value of $N_{\text{H}} = 1.7 \times 10^{21} \text{ cm}^{-2}$ obtained from the spectrum of the pulsar, but the photon index range remains the same (Fig. 11, bottom). We also attempted to fit the spectra from the PWN region farther down the tail, to see if there is any indication of spectral softening, but the number of photons from this faint part of the nebula is too small for a meaningful spectral analysis.

The PWN flux, $F_{\text{PWN}} = 2.1\text{--}3.6 \times 10^{-14}$, determined from the elliptical region, is poorly constrained because of the low statistics. We also measured a flux of $3.4 - 5.8 \times 10^{-14} \text{ ergs cm}^{-2} \text{ s}^{-1}$ from the whole visible PWN. The unabsorbed luminosity of the whole nebula estimated from this observed flux is $L_{\text{PWN}} = 5.3\text{--}8.6 \times 10^{29} \text{ ergs s}^{-1}$, in the 0.3–8 keV band.

The absorption column determined from the spectral fit of the nebula is significantly lower than that determined from the PL fit of the pulsar spectrum, but it is in a good agreement with the value derived from the PL+BB model. This further supports our detection of the thermal component in the spectrum of B1929.

3. Discussion and conclusions

3.1. The nebula around PSR B1929+10

3.1.1. PWN morphology

In the analysis of the two ACIS-S observations of B1929, we detected a faint PWN surrounding this old pulsar. We found that the pulsar is immersed in a very compact, $\approx 9'' \times 5''$ nebula elongated in the direction perpendicular to the pulsar’s proper motion (Fig. 1, bottom). Together with the two patchy “wings” (best seen in slightly smoothed

images), the overall compact structure looks like a bow shock PWN, with an apex at $\approx 3''$ ($\approx 1.6 \times 10^{16}$ cm at $d = 361$ pc) ahead of the pulsar. In addition, there is marginal evidence of a short jet-like feature emerging from the pulsar between the wings, in the direction opposite to the pulsar’s proper motion (seen up to $3''$ – $4''$ from the pulsar in the unsmoothed combined image and in the pulsar-subtracted image in Fig. 1). There is also some very faint emission in front of the apparent bow-shock apex, seen up to $6''$ – $7''$ from the pulsar (see Fig. 4).

In addition to the compact PWN, a faint, inhomogeneous tail-like structure was detected, extending in the direction approximately opposite to the pulsar’s proper motion up to at least $\sim 1.5'$ – $2'$. This structure is well aligned with the much longer tail (up to $10'$ – $15'$) detected in the *ROSAT* and *XMM-Newton* data (Wang et al. 1993; Becker et al. 2006).

The surface brightness of the detected PWN is not uniform: e.g., the two wings are brighter than the other PWN structures (see Table 2). Furthermore, the *Chandra* and *XMM-Newton* data suggest a possible variability of the detected PWN, although the number of detected photons was too small to establish it unambiguously.

The approximate axial symmetry with respect to the direction of the pulsar’s proper motion strongly suggests that the PWN is shaped by the oncoming flow of the ambient matter in the pulsar’s reference frame. The corrected pulsar’s proper motion and distance correspond to the pulsar’s speed $v_{\text{PSR}} = 178 (\sin i)^{-1}$ km s $^{-1}$, where i is the angle between the velocity vector and the line of sight. It exceeds the ISM sound speed, $c_s = (5kT/3\mu m_H)^{1/2} = 37\mu^{-1/2}T_5^{1/2}$ km s $^{-1}$ (where μ is the molecular weight, $T_5 = T/10^5$ K), for $T < 2.3 \times 10^6\mu (\sin i)^{-2}$ K, i.e., for virtually any plausible ISM temperature, which supports the bow-shock interpretation of the detected nebular emission.

Our current understanding of the pulsar wind dynamics in a bow-shock PWN mostly relies upon numerical models. A recent work in this direction has been done by van der Swaluw (2003), Bucciantini et al. (2005), and Vigelius et al. (2007). These models show that at supersonic pulsar speeds the termination shock (TS) of an *isotropic* pulsar wind acquires a bullet-like shape, with a distance

$$R_h \simeq (\dot{E}/4\pi c p_{\text{ram}})^{1/2} \quad (1)$$

between the pulsar and the bullet head, where

$$p_{\text{ram}} = \rho_{\text{amb}} v_{\text{PSR}}^2 \quad (2)$$

is the ram pressure, and ρ_{amb} is the ambient density. The shocked pulsar wind is confined between the TS and the contact discontinuity (CD) surface, while the forward bow shock (FBS) separates the shocked ambient medium (between the CD and the FBS) from the unshocked one. For large Mach numbers, $\mathcal{M} \equiv v_{\text{PSR}}/c_s = (3p_{\text{ram}}/5p_{\text{amb}})^{1/2} \gg 1$, and small

values of the magnetization parameter⁶ of the pre-shock pulsar wind, $\sigma < 0.1$, the bullet’s cylindrical radius is $r_{\text{TS}} \sim R_h$ and the distance of its back surface from the pulsar is $R_b \sim 6R_h$ (see Figs. 1–3 in Bucciantini et al. 2005). The shape of the CD surface ahead of the pulsar is similar to that of the TS but with the apex at $R_{\text{CD}} \approx 1.3R_h$, while it acquires a cylindrical shape with a radius $r_{\text{CD}} \approx 4R_h$ behind the TS bullet. The shocked wind flows away from the pulsar within this cylinder, forming a PWN tail. The flow velocity in the central part of the tail (the inner channel, $r \lesssim r_{\text{TS}}$) is $\sim 0.1c$ – $0.2c$, while it is as high as $v_{\text{tail}} = 0.8c$ – $0.9c$ in the bulk of the tail’s volume, at $r_{\text{TS}} \lesssim r < r_{\text{CD}}$ (where r is the cylindrical radius). The magnetic field, purely toroidal in these models, also depends on r , being enhanced toward the tail axis and the CD surface. Its typical value in the tail is

$$B_{\text{tail}} \sim 2.8 (c/v_{\text{tail}}) (\sigma p_{\text{ram}})^{1/2} \text{G}, \quad (3)$$

where the p_{ram} is in units of dyn cm^{-2} (see eq. (13) of Bucciantini et al. 2005). In the numerical simulations, the flow velocity and the magnetic field do not show substantial changes along the tail, but these simulations are limited to relatively short distances from the pulsar (e.g., $< 13R_h$ in Bucciantini et al. 2005).

To interpret the B1929 PWN in the framework of the current MHD models, we attempted to match the observed morphological structures with those predicted by the simulations. As the brightest X-ray emission is expected from the shocked wind between the TS and CD in the front part of the PWN, we assume that the very compact structure in the immediate vicinity of the pulsar (Fig. 1, bottom) is the PWN head and estimate the distance from the pulsar to the CD apex to be $\sim 3''$. This corresponds to $R_{\text{CD}} \sim 1.6 \times 10^{16}$ cm, $R_h \sim r_{\text{TS}} \sim 1.2 \times 10^{16}$ cm (or $2.3''$), $R_b \sim 7.5 \times 10^{16}$ cm (or $14''$), and $r_{\text{CD}} \sim 4.8 \times 10^{16}$ cm (or $9''$). In this picture, the patchy wings in the PWN image are produced by the shocked wind between the TS and CD, while the “blobs” farther behind the pulsar are in the pulsar tail. However, the faint emission ahead of the pulsar (region 3, or the Front, in Fig. 1, top, and Table 2) is not explained in this model. We can only speculate that this emission might be produced by a polar outflow along the pulsar’s spin axis (not included in the models), possibly scattered by the head wind, or it might suggest that, because of the Rayleigh-Taylor instability, the CD surface acquires an irregular shape ahead of the pulsar, with “fingers” of the shocked wind penetrating into the shocked ISM. As the above estimates of sizes of the PWN elements are based on simplified models and shallow images, one should consider them as order-of-magnitude estimates rather than accurately established values. Therefore, in the following estimates, we will retain the explicit dependence on R_h , scaling it as $R_h = R_{h,16} \times 10^{16}$ cm.

⁶The magnetization parameter in the pre-shock wind is defined as the ratio of the Poynting flux to the kinetic energy flux.

Using this estimate for R_h and equation (1), we can calculate the ram pressure:

$$p_{\text{ram}} = \dot{E} f_{\Omega} (4\pi c R_h^2)^{-1} = 1.0 \times 10^{-10} f_{\Omega} R_{h,16}^{-2} \text{ dyn cm}^{-2}, \quad (4)$$

where we introduced the factor f_{Ω} to account for possible anisotropy of the pulsar outflow (e.g., $f_{\Omega} < 1$ for a mostly equatorial outflow if the equatorial plane is perpendicular to the pulsar’s velocity). Since, on the other hand,

$$p_{\text{ram}} = \rho_{\text{amb}} V_{\text{PSR}}^2 = 5.3 \times 10^{-10} n_{\text{amb}} (\sin i)^{-2} \text{ dyn cm}^{-2}, \quad (5)$$

where $n_{\text{amb}} \equiv \rho_{\text{amb}}/m_H$, we obtain an estimate for the ambient number density:

$$n_{\text{amb}} = 0.19 f_{\Omega} R_{h,16}^{-2} \sin^2 i \text{ cm}^{-3}. \quad (6)$$

Using equation (4), we can estimate the Mach number:

$$\mathcal{M} = 7.7 f_{\Omega}^{1/2} R_{h,16}^{-1} p_{\text{amb},-12}^{-1/2}, \quad (7)$$

where we scaled p_{amb} to $10^{-12} \text{ dyn cm}^{-2}$, a typical value for the ISM. From the corresponding sound speed, $c_s = 23 f_{\Omega}^{-1/2} R_{h,16} p_{\text{amb},-12}^{1/2} (\sin i)^{-1} \text{ km s}^{-1}$, we estimate the temperature:

$$T = 3.9 \times 10^4 \mu f_{\Omega}^{-1} R_{h,16}^2 p_{\text{amb},-12} (\sin i)^{-2} \text{ K}. \quad (8)$$

The ambient pressure in the unperturbed ISM is in the range $p_{\text{amb},-12} \approx 0.2\text{--}2$ (Heiles 2001; Ferrière 2001). The pressure in the pulsar’s neighborhood might be somewhat higher if the pulsar’s UV and soft X-ray emission heats and ionizes the surrounding medium, which is supported by the lack of an H_{α} bow-shock PWN in the observations reported by Becker et al. (2006) (see Bucciantini & Bandiera 2001, for a detailed discussion on conditions of observability of H_{α} bow-shock PWNs). As the factor $\mu f_{\Omega}^{-1} R_{h,16}^2 (\sin i)^{-2}$ is also very likely greater than unity, we expect $T \sim 10^5 \text{ K}$ to be a realistic estimate for the ambient temperature.

We should note that although the comparison of our data with the numerical models leads to reasonable estimates for the parameters of the ambient medium, these two-dimensional models are based on a number of assumptions that are not necessarily realistic. In particular, the models assume an isotropic pulsar outflow, whereas we know that it is predominantly equatorial, at least in the case of young pulsars. Obviously, a substantial anisotropy would distort the shape of the bow shock in the pulsar vicinity (e.g., decreasing R_h in the case of an equatorial outflow in the plane perpendicular to the pulsar velocity). For B1929, a hint of an equatorial outflow might be suggested by the elongation of the most compact PWN structure perpendicular to the proper motion (Fig. 1, bottom). Such a structure, together with the “wings”, might be interpreted as a torus of the shocked equatorial

wind, compressed and possibly bent by the oncoming wind. Such an interpretation might also be supported by the marginal detection of the jet-like structure immediately behind the pulsar and the faint emission ahead of the pulsar (a crushed counter-jet?).

Application of the PWN simulations to the observed tail leads to some discrepancies. For instance, although the tail may look like a cylinder with the predicted diameter of $\sim 18''$ at the relatively small distances, $\lesssim 2'$, from the pulsar in the ACIS images, its transverse size apparently increases at larger distances, possibly reaching $\sim 5'$ at the edge of the MOS field of view ($15'$ from the pulsar). The tail's surface brightness looks very patchy, which might suggest some interaction of the shocked wind with the surrounding medium, such as the Kelvin-Helmholtz instability caused by the shear at the CD surface. This instability may produce clumps of shocked ISM embedded in the shocked wind, which would distort the flow pattern and compress the wind material (Bucciantini et al. 2005). The same instability may result in temporal variations in the X-ray emission of the tail, with a time scale of $r_{\text{CD}}/c \sim 0.5$ months, which might explain the alleged variability of the PWN (§ 2.1.2).

Using equations (3) and (4), the magnetic field in the tail can be estimated as

$$B_{\text{tail}} = 56\sigma^{1/2}(0.5c/v_{\text{tail}})f_{\Omega}^{1/2}R_{h,16}^{-1} \mu\text{G}. \quad (9)$$

We should note that this field becomes rather small, comparable to the interstellar magnetic field, at the usually assumed small values of the magnetization parameter, $\sigma \lesssim 10^{-2}$.

Using this estimate of B_{tail} , we can estimate the synchrotron cooling time for relativistic electrons in the tail, $\tau_{\text{syn}} = 5.1 \times 10^{10}\gamma_8^{-1}B_{-5}^{-2}$ s, where $\gamma = 10^8\gamma_8$ is the electron Lorentz factor and $B_{-5} = B/10^{-5}$ G. As the characteristic energy of synchrotron photons is

$$E \sim 0.5B_{-5}\gamma_8^2 \text{ keV}, \quad (10)$$

photons with energy E are emitted by electrons with $\gamma_8 \sim 2(E/1 \text{ keV})^{1/2}B_{-5}^{-1/2}$, and the synchrotron cooling time corresponding to $E = 8$ keV photons (upper energy of our band) is

$$\tau_{\text{syn}} = 6.8 \times 10^8(\sigma f_{\Omega})^{-3/4}(v_{\text{flow}}/0.5c)^{3/2}(E/8 \text{ keV})^{-1/2}R_{h,16}^{3/2} \text{ s}. \quad (11)$$

It follows from this equation that the projected tail length, $l_{\text{tail}} \sim v_{\text{flow}}\tau_{\text{syn}} \sin i$, as observed at energy E , can be estimated as

$$l_{\text{tail}} \sim 1 \times 10^{19} \left(\frac{v_{\text{flow}}}{0.5c}\right)^{5/2} \left(\frac{8 \text{ keV}}{E}\right)^{1/2} \left(\frac{R_{h,16}^2}{\sigma f_{\Omega}}\right)^{3/4} \sin i \text{ cm}. \quad (12)$$

For instance, for $\sigma = 0.01$, $R_{h,16}f_{\Omega}^{-1/2} = 2$, $v_{\text{flow}} = 0.5c$, $\sin i = 0.5$, and $E < 8$ keV we obtain $l_{\text{tail}} \gtrsim 150$ pc (i.e., $\sim 24^\circ$), two orders of magnitude larger than observed by *XMM-Newton*

and *ROSAT*. The main reason for this discrepancy is the assumption that the flow speed remains very high along the entire tail in the ideal MHD model. Bucciantini et al. (2005) have noticed that a similar discrepancy arises when the same model is applied to the X-ray tail of the Mouse PWN: the observed tail length is much shorter than that estimated from the model at any $\sigma < 1$. These authors suggest that the flow can be slowed down by the interaction with the ambient medium, which could also explain the divergence of the Mouse tail in the radio. As these factors have not been included in the current models, we can only empirically estimate an average flow velocity that would be consistent with the observed length of 1.5 pc: $v_{\text{flow}} \sim 0.1c \sigma_{-2}^{3/10} (f_{\Omega}/R_{h,16}^2)^{3/10} (\sin i)^{-2/5}$, assuming that equation (3) is still applicable (here $\sigma_{-2} = \sigma/10^{-2}$). We note that this velocity is still much larger than the pulsar velocity. This means that the equation

$$l_{\text{tail}} = v_{\text{PSR},\perp} \tau_{\text{syn}} \approx 0.3 (v_{\text{PSR},\perp}/178 \text{ km s}^{-1}) \gamma_8^{-1} B_{-5}^{-2} \text{ pc}, \quad (13)$$

often used for estimating the magnetic field (e.g., Becker et al. 2006), is inapplicable in this case⁷.

It is worthwhile to mention that the length of the tail of B1929 measured so far might be limited by the field of view of the available *XMM-Newton* observations, and further deep observations along the tail are needed to determine its full extent. Recent observations with *Chandra* and *XMM-Newton* have discovered a number of other PWNe with very long tails (Kargaltsev & Pavlov 2008), including the 6 pc tail ($l_{\text{tail}}/R_h \sim 600$) behind PSR J1509–5850, the longest pulsar tail known to date (Kargaltsev et al. 2008). Detection of more such objects would help to facilitate further modeling that would account for cooling in the varying magnetic field at larger distances from the pulsar.

3.1.2. X-ray luminosity and spectrum of the PWN

From our estimate of the total unabsorbed flux of the B1929 PWN detected with *Chandra*, we estimated the X-ray PWN luminosity, $L_{\text{PWN}} = (5.3\text{--}8.6) \times 10^{29} \text{ ergs s}^{-1}$, which corresponds to the PWN efficiency $\eta_{\text{PWN}} \equiv L_{\text{PWN}}/\dot{E} = (1.4\text{--}2.2) \times 10^{-4}$ in the 0.3–8 keV band. Similar values of the luminosity and efficiency have been measured in the *XMM-Newton*

⁷Equation (13) implies that the shocked wind flow acquires the speed of the ambient ISM matter in the immediate vicinity of the pulsar, so that the observed elongated PWN is actually a “trail” of the decelerated wind left behind the moving pulsar. Such an assumption strongly contradicts all the models of bow-shock PWNe (e.g., Romanova et al. 2005; Bucciantini et al. 2005). Becker et al. (2006) obtained a reasonable estimate for the magnetic field, $B \lesssim 12 \mu\text{G}$, using eq. (13) because they assumed $\gamma = 10^6$. However, at such B and γ , the energy of a synchrotron photon is $E = 6 \text{ eV}$ (see eq. [10]), well below the X-ray band.

data by Becker et al. (2006) from a larger area farther southwest from the pulsar. As both measurements were taken for small fractions of the PWN, the luminosity and efficiency of the entire PWN can be higher than these estimates.

The estimated efficiency of the B1929 PWN is within the range $\eta_{\text{PWN}} \sim 10^{-4.5}-10^{-2}$ found by Kargaltsev et al. (2007) in a recent study of several energetic middle-aged Vela-like pulsars and their PWNe. Compared to a few known PWNe with long tails, which, on average, show higher efficiencies, $\eta_{\text{PWN}} \sim 10^{-3.8}-10^{-1.7}$, than more compact PWNe (see Kargaltsev et al. 2008), the B1929 PWN is among the least efficient ones; however, we stress that a deeper observation of B1929 is needed to measure the efficiency more accurately.

The spectral slope of the PWN spectrum is also consistent with the values measured for other PWNe (e.g., see Kargaltsev et al. 2007; Kargaltsev & Pavlov 2008).

3.2. Spectral properties of PSR B1929+10

As we mention in §1, it has been a matter of debate whether the X-ray emission from B1929 is predominantly magnetospheric or it has a significant thermal component emitted from the neutron star surface. Most recently, Becker et al. (2006) have concluded, based on the analysis of the *XMM-Newton* data, that the spectrum of B1929 is best described by a PL model (i.e. the emission is predominantly magnetospheric), while the contribution of the thermal component, modeled as BB radiation, does not exceed $\sim 7\%$. Our analysis of the *Chandra* and *XMM-Newton* spectra has shown, however, that adding the BB component to the PL model significantly improves the fit to the combined *Chandra* plus *XMM-Newton* spectrum, with the the best-fit BB component providing $\sim 45\%$ of the luminosity in the 0.3–10 keV band.

In addition to the better fit, there are other serious arguments in favor of the PL+BB model. First of all, the hydrogen column density, $N_{\text{H}} = (2.23 \pm 0.27) \times 10^{21} \text{ cm}^{-2}$, obtained from the PL fit, looks unreasonably large. In particular, it is much larger than the standard estimate, $N_{\text{H}} \sim 10N_e \approx 1 \times 10^{20} \text{ cm}^{-2}$, obtained from the pulsar’s dispersion measure, $\text{DM} = 3.178 \text{ pc cm}^{-3}$, under the usual assumption of a 10% ISM ionization (where N_e is the electron column density). In other words, the PL model requires a very low ISM ionization, $\sim 0.4\%$, (i.e., a very large ratio $N_{\text{H}}/N_e \sim 230$, much larger than for any other radio pulsar detected in X-rays). Also, taking into account that B1929 is a nearby pulsar ($d = 361 \text{ pc}$), the N_{H} obtained from the PL fit is uncomfortably close to the HI column density, $N_{\text{HI}} = 3.5 \times 10^{21}$, throughout the entire Galaxy in the direction of B1929 (Kalberla et al. 2005). On the contrary, $N_{\text{H}} = 0.17^{+0.23}_{-0.17} \times 10^{21} \text{ cm}^{-2}$ inferred from the PL+BB fit is consistent

with the usual estimate based on the dispersion measure as well as with the N_{H} estimated from the PWN spectrum (see Fig. 11), and it is much lower than the total Galactic N_{HI} .

Also, the PL+BB model looks more attractive than the PL model because it gives the slope of the PL component, $\Gamma \approx 1.7$, within the range of spectral slopes found for a large sample of young pulsars ($\Gamma \approx 1-2$; Gotthelf 2003), while the PL fit to the B1929 spectrum results in a considerably steeper slope, $\Gamma \approx 3$. One could argue that the PL fits to the spectra of other old pulsars (e.g., B0950+08, B2224+65, B0823+26, B0628-28, B1133+16, B0943+10; Zavlin & Pavlov 2004; Becker et al. 2004; Tepedelenhoğlu & Ögelman 2005; Kargaltsev et al. 2006; Zhang et al. 2005) also show rather steep slopes, $\Gamma \approx 2-3$, suggesting that pulsar spectra might soften with increasing age or decreasing spin-down power (Kargaltsev et al. 2006). However, a plausible alternative interpretation of the softer spectra of old pulsars is that they are, in fact, comprised of a (soft) thermal component and a PL component with a more gradual slope⁸, similar to those found in young pulsars (Zavlin & Pavlov 2004).

Thus, based on the goodness of fit and the astrophysical arguments, we conclude that the X-ray emission from B1929 most likely includes both thermal and magnetospheric components. The BB model for the thermal component gives the apparent temperature $kT_a \approx 0.3 \text{ keV}$ and projected emitting area $A_{\perp,a} \sim 3000 \text{ m}^2$, at the distance of 361 pc, suggesting that the thermal emission originates from small heated spots (e.g., polar caps). These temperature and area correspond to the apparent radius $R_a^{\text{es}} = (A_{\perp,a}/\pi)^{1/2} \approx 33 \text{ m}$ and bolometric luminosity $L_{\text{bol},a}^{\text{es}} = 4A_{\perp,a}\sigma T_a^4 \approx 1.1 \times 10^{30} \text{ ergs s}^{-1}$ of an equivalent sphere. The true size and luminosity of the polar caps depend on the geometry and the gravitational redshift factor, $g_r = (1 - R_g/R_{\text{NS}})^{1/2}$, where $R_g = 2.95M_{\text{NS}}/M_{\odot} \text{ km}$, R_{NS} and M_{NS} are the mass and radius of the neutron star. If there are two identical hot spots at the poles of a centered magnetic dipole, the polar cap radius and the luminosity of two polar caps, as measured at the neutron star surface, are $R_{\text{pc}} = R_a^{\text{es}} f^{-1/2}$ and $L_{\text{bol,pc}} = L_{\text{bol},a}^{\text{es}}/(2fg_r^4)$, where $f \leq 1$ is a geometrical factor depending on the angles ζ between the line of sight and the spin axis and α between the spin and magnetic axes, as well as on g_r (Pavlov et al. 2007). For instance, assuming $M_{\text{NS}} = 1.4M_{\odot}$, $R_{\text{NS}} = 10 \text{ km}$ (i.e. $g_r = 0.766$), $\alpha = 36.0^\circ$, and $\zeta = 61.5^\circ$ (Everett & Weisberg 2001) and using the approach described by Zavlin et al. (1995) and Beloborodov (2002), we find $f = 0.897$, which gives $R_{\text{pc}} = 1.06R_a^{\text{es}} \approx 35 \text{ m}$ and $L_{\text{bol,pc}} = 1.62L_{\text{bol},a}^{\text{es}} \approx 1.8 \times 10^{30} \text{ ergs s}^{-1} = 4.7 \times 10^{-4}\dot{E}$.

The estimated polar cap radius is a factor of ~ 9 smaller than the conventional polar cap radius of a radio pulsar, $\tilde{R}_{\text{pc}} = (2\pi R_{\text{NS}}^3/cP)^{1/2}$ (see e.g., Michel 1991), which is \approx

⁸Note that the observed spectra of these pulsars can be satisfactorily fitted with quite different models because these objects are very faint in the X-ray range.

300 m for B1929, assuming $R_{\text{NS}} = 10$ km. However, the observed polar cap radii can be substantially smaller or larger than the conventional value. In particular, BB fits of several old pulsar spectra show $R_{\text{pc}} \sim (0.1\text{--}0.2) \tilde{R}_{\text{pc}}$ (e.g., Zavlin & Pavlov 2004; Zhang et al. 2005; Kargaltsev et al. 2006). For some pulsars, such a discrepancy can be alleviated assuming that the polar cap is covered by a hydrogen or helium atmosphere, in which case the effective temperature would be a factor of 2 lower, and the radius a factor of 3–10 larger while the bolometric luminosity would not change significantly (Pavlov et al. 1995; Zavlin & Pavlov 2004). Another explanation for such a discrepancy was proposed by Zhang et al. (2005), who suggested that only a small fraction of the polar cap surface, associated with footprints of sparks produced by intermittent breakdowns of an “inner gap” above the polar cap, is hot enough to emit X-rays.

The luminosity of the detected thermal component, which is less dependent on the assumed spectral model than the radius and temperature, can be compared with the models for pulsar polar cap heating (Harding & Muslimov 2002, 2001). For B1929, these models predict the polar cap luminosity $L_{\text{bol,pc}} \sim 10^{31}$ ergs s⁻¹ if the polar cap is heated by positrons produced through curvature radiation of electrons accelerated in the neutron star magnetosphere. Although the polar cap thermal luminosity estimated from the PL+BB spectral model is a factor of a few lower than that predicted by Harding & Muslimov (2001), this can be considered as a reasonably good agreement, with account of the uncertainties of both the theoretical model and the observational results. We expect that deeper observations of other old pulsars would also detect thermal components from their polar caps and help us better understand the polar cap heating mechanisms.

As Figure 8 shows, the thermal component dominates at $0.5 \text{ keV} \lesssim E \lesssim 2 \text{ keV}$. This means that we can expect different pulse shapes within and outside this energy range, because the pulsations of thermal radiation should be smoother and shallower than those of the magnetospheric radiation. The study of the energy dependence of pulsations not only can confirm the presence of the thermal component, but it would also allow one to infer the polar cap geometry and emission mechanism (e.g., BB vs. a light-element atmosphere), and even measure the mass-to-radius ratio for the neutron star (Zavlin et al. 1995; Pavlov & Zavlin 1997; Zavlin & Pavlov 2004). Since the current *XMM-Newton* data with sufficient time resolution do not have enough counts for such an analysis, a new deep observation of B1929 is needed to perform this important test.

The spectral slope of the PL (magnetospheric) component inferred from the PL+BB fit is $\Gamma \approx 1.7$, similar to those of younger pulsars. The luminosity of this component, $L_X = 4\pi d^2 F_X^{\text{unabs}} \approx 1.7 \times 10^{30}$ ergs s⁻¹ in the 0.3–10 keV band, corresponds to the nonthermal X-ray efficiency $\eta_{\text{nonth}} = L_X / \dot{E} \approx 4.4 \times 10^{-4}$, typical for the whole population of radio pulsars

detected in the X-rays, and comparable to the thermal (polar cap) efficiency. Notice that the one-component PL fit results not only in a much softer spectrum ($\Gamma \approx 3.0$) but also in a higher luminosity, $L_X \approx 6.6 \times 10^{30}$ ergs s^{-1} , and efficiency, $\eta_{\text{month}} \approx 1.7 \times 10^{-3}$, above the typical value for X-ray emitting radio pulsars. A similar trend has been observed in other old pulsars: PL fits of their spectra yield X-ray efficiencies noticeably higher than those of young and middle-aged pulsars, which might suggest that the X-ray efficiency in this energy range grows with increasing age and decreasing spin-down power, perhaps at the expense of the efficiency at higher photon energies. However, this conclusion is based on the assumption that the contribution of the thermal component is negligible in the soft X-ray range, which we believe is not valid at least for the best-studied old pulsars, B1929 and B0950+08. To understand the evolution of X-ray properties of pulsars, deep observations of a larger sample of old pulsars are warranted.

3.3. Summary

Two ACIS-S observations of B1929 revealed a faint PWN surrounding this old, nearby pulsar. The observed morphology includes a compact nebula with two patchy wings in the immediate vicinity of B1929, and a tail extending in the direction opposite to the pulsar's proper motion, aligned with the much longer tail detected in the previous *ROSAT* and *XMM-Newton* observations. The shape of the nebula and its spectral properties are consistent with the proposed bow-shock classification. The properties of the compact nebula suggest that the pulsar wind outflow is anisotropic, possibly concentrated toward the equatorial plane perpendicular to the pulsar velocity. The size of the observed tail implies an average flow velocity of $\sim 0.1c$. The whole observed PWN radiates about 2×10^{-4} of the pulsar spin-down power in X-rays. By comparing the observed PWN properties with the bow-shock MHD models, we estimated the temperature of the local ISM to be $\sim 10^5$ K, which is consistent with the lack of the $H\alpha$ bow-shock emission around this pulsar.

In the spectral analysis of the combined *Chandra* and *XMM-Newton* data, we detected a thermal component in the pulsar radiation, whose luminosity, $\sim (1-2) \times 10^{30}$ ergs s^{-1} , is comparable with the magnetospheric luminosity in the X-ray band. The thermal radiation is likely emanating from polar caps heated by positrons created by the curvature radiation of ultrarelativistic electrons accelerated in the pulsar magnetosphere. The spectrum and X-ray efficiency of the magnetospheric component are similar to those found in young and middle-aged pulsars. Further X-ray observations of the pulsar will allow one to better characterize its spectral and timing properties and understand the nature of the magnetospheric radiation and the mechanisms of polar cap heating.

We thank Patric Broos for the useful discussion about the MARX simulations, Oleg Kargaltsev and Leisa Townsley for the help with the high-resolution imaging techniques, and Slava Zavlin for the discussion about the *XMM-Newton* spectral results. We would also like to thank the referee for very helpful comments and suggestions. This work was partially supported by NASA grant NAG5-10865 and *Chandra* award SV4-74018.

REFERENCES

- Becker, W., Jessner, A., Kramer, M., Testa, V., & Howaldt, C. 2005, *ApJ*, 633, 367
- Becker, W., et al. 2006, *ApJ*, 645, 1421
- Becker, W., & Trümper, J. 1997, *A&A*, 326, 682
- Becker, W., Weisskopf, M. C., Tennant, A. F., Jessner, A., Dyks, J., Harding, A. K., & Zhang, S. N. 2004, *ApJ*, 615, 908
- Beloborodov, A. M. 2002, *ApJ*, 566, L85
- Binney, J., & Tremaine, S. 1987, *Galactic dynamics* (Princeton, NJ, Princeton University Press)
- Boesgaard, A. M., & Tripicco, M. J. 1986, *ApJ*, 303, 724
- Bucciantini, N., Amato, E., & Del Zanna, L. 2005, *A&A*, 434, 189
- Bucciantini, N., & Bandiera, R. 2001, *A&A*, 375, 1032
- Caraveo, P. A., Bignami, G. F., De Luca, A., Pellizzoni, A., Mereghetti, S., Mignani, R. P., Tur, A., & Becker, W. 2004, *Memorie della Societa Astronomica Italiana*, 75, 470
- Chatterjee, S., Cordes, J. M., Vlemmings, W. H. T., Arzoumanian, Z., Goss, W. M., & Lazio, T. J. W. 2004, *ApJ*, 604, 339
- Cutri, R. M., et al. 2003, 2MASS All Sky Catalog of point sources. (The IRSA 2MASS All-Sky Point Source Catalog, NASA/IPAC Infrared Science Archive. <http://irsa.ipac.caltech.edu/applications/Gator/>)
- Del Zanna, L., Amato, E., & Bucciantini, N. 2004, *A&A*, 421, 1063
- Everett, J. E., & Weisberg, J. M. 2001, *ApJ*, 553, 341
- Ferrière, K. M. 2001, *Reviews of Modern Physics*, 73, 1031

- Gaensler, B. M., Stappers, B. W., Frail, D. A., & Johnston, S. 1998, *ApJ*, 499, L69
- Gaensler, B. M., van der Swaluw, E., Camilo, F., Kaspi, V. M., Baganoff, F. K., Yusef-Zadeh, F., & Manchester, R. N. 2004, *ApJ*, 616, 383
- Gotthelf, E. V. 2003, *ApJ*, 591, 361
- Harding, A. K., & Muslimov, A. G. 2001, *ApJ*, 556, 987
- Harding, A. K., & Muslimov, A. G. 2002, *ApJ*, 568, 862
- Heiles, C. 2001, *ApJ*, 551, L105
- Helfand, D. J. 1983, in *IAU Symp. 101: Supernova Remnants and their X-ray Emission*, ed. J. Danziger & P. Gorenstein, 471
- Hester, J. J., et al. 2002, *ApJ*, 577, L49
- Johnson, D. R. H., & Soderblom, D. R. 1987, *AJ*, 93, 864
- Kalberla, P. M. W., Burton, W. B., Hartmann, D., Arnal, E. M., Bajaja, E., Morras, R., & Pöppel, W. G. L. 2005, *A&A*, 440, 775
- Kargaltsev, O., Misanovic, Z., Pavlov, G. G., Wong, J. A., & Garmire, G. P. 2008, *ArXiv* 0802.2963
- Kargaltsev, O., & Pavlov, G. G. 2008, in *American Institute of Physics Conference Series*, Vol. 983, *40 Years of Pulsars: Millisecond Pulsars, Magnetars and More*, 171
- Kargaltsev, O., Pavlov, G. G., & Garmire, G. P. 2006, *ApJ*, 636, 406
- Kargaltsev, O., Pavlov, G. G., & Garmire, G. P. 2007, *ApJ*, 660, 1413
- Kargaltsev, O., Pavlov, G. G., Sanwal, D., Wong, J., & Garmire, G. P. 2006, in *Bulletin of the American Astronomical Society*, Vol. 38
- Kawai, N., Tamura, K., & Saito, Y. 1998, *Advances in Space Research*, 21, 213
- Komissarov, S. S., & Lyubarsky, Y. E. 2003, *MNRAS*, 344, L93
- McGowan, K. E., Vestrand, W. T., Kennea, J. A., Zane, S., Cropper, M., & Córdova, F. A. 2007, *Ap&SS*, 308, 309
- Michel, F. C. 1991, *Theory of neutron star magnetospheres* (Univ. of Chicago Press, 1991, 533)

- Misanovic, Z., Pavlov, G. G., & Garmire, G. P. 2006, in *Bulletin of the American Astronomical Society*, Vol. 38
- Monet, D. G., et al. 2003, *AJ*, 125, 984
- Moon, D.-S., et al. 2004, *ApJ*, 610, L33
- Mori, K., Tsunemi, H., Miyata, E., Baluta, C. J., Burrows, D. N., Garmire, G. P., & Chartas, G. 2001, in *ASP Conf. Ser. 251: New Century of X-ray Astronomy*, ed. H. Inoue & H. Kunieda, 576
- Pavlov, G. G., Kargaltsev, O., Garmire, G. P., & Wolszczan, A. 2007, *ApJ*, 664, 1072
- Pavlov, G. G., Sanwal, D., & Zavlin, V. E. 2006, *ApJ*, 643, 1146
- Pavlov, G. G., Shibanov, Y. A., Zavlin, V. E., & Meyer, R. D. 1995, in *The Lives of the Neutron Stars. Proceedings of the NATO Advanced Study Institute on the Lives of the Neutron Stars*, ed. M. A. Alpar, U. Kiziloglu, & J. van Paradijs, 71
- Pavlov, G. G., Teter, M. A., Kargaltsev, O., & Sanwal, D. 2003, *ApJ*, 591, 1157
- Pavlov, G. G., & Zavlin, V. E. 1997, *ApJ*, 490, L91
- Romani, R. W., & Ng, C.-Y. 2003, *ApJ*, 585, L41
- Romanova, M. M., Chulsky, G. A., & Lovelace, R. V. E. 2005, *ApJ*, 630, 1020
- Słowikowska, A., Kuiper, L., & Hermsen, W. 2005, *A&A*, 434, 1097
- Stappers, B. W., Gaensler, B. M., Kaspi, V. M., van der Klis, M., & Lewin, W. H. G. 2003, *Science*, 299, 1372
- Tepedelenhoğlu, E., & Ögelman, H. 2005, *ApJ*, 630, L57
- Tsunemi, H., Mori, K., Miyata, E., Baluta, C., Burrows, D. N., Garmire, G. P., & Chartas, G. 2001, *ApJ*, 554, 496
- van der Swaluw, E. 2003, *A&A*, 404, 939
- Vigelius, M., Melatos, A., Chatterjee, S., Gaensler, B. M., & Ghavamian, P. 2007, *MNRAS*, 374, 793
- Wang, F. Y.-H., & Halpern, J. P. 1997, *ApJ*, 482, L159
- Wang, Q. D., Li, Z.-Y., & Begelman, M. C. 1993, *Nature*, 364, 127

Weisskopf, M. C., et al. 2000, ApJ, 536, L81

Yancopoulos, S., Hamilton, T. T., & Helfand, D. J. 1994, ApJ, 429, 832

Zavlin, V. E., & Pavlov, G. G. 2004, ApJ, 616, 452

Zavlin, V. E., Shibano, Y. A., & Pavlov, G. G. 1995, Astronomy Letters, 21, 149

Zhang, B., Sanwal, D., & Pavlov, G. G. 2005, ApJ, 624, L109

Table 1: *Chandra* and *XMM-Newton* observations of B1929

Instrument	Obs ID	Date	Exposure
EPIC	0113051301	10 Nov 2003	10.5 / 10.5 / 7.3
EPIC	0113051401	27 Apr 2004	15.2 / 16.4 / 11.0
EPIC	0113051501	29 Apr 2004	7.3 / 7.6 / 10.3
ACIS	6657	4 Dec 2005	20.9
ACIS	7230	28 May 2006	24.6

Note. — The good-time exposures are given in ks. The first, second, and third EPIC exposures are for MOS1, MOS2, and PN, respectively. The effective PN exposure in each observation is $\sim 70\%$ of the total PN good-time exposure because of the reduced efficiency of the small window mode.

Table 2: Background-subtracted counts and surface brightness of PWN regions in *Chandra* observations 6657, 7230, and combined data

Region		1 (Southern Wing)	2 (Northern Wing)	3 (Front)	4 (Inner Blob)	5 (Outer Blob)
Extraction area arcsec ²		31.5	46.7	77.9	157	1884
Counts (bkg-subtracted)	6657	18.9±4.6	6.9±3.2	12.7±4.2	23.5±5.8	57±14
	7230	15.3±4.1	17.3±4.5	3.7±2.8	14.4±4.8	116±15
	comb.	34.1±6.1	24.1±5.5	16.4±5.0	37.9±7.7	173±20
Bkg-subtracted surface brightness (10 ⁻⁵ cts s ⁻¹ arcsec ⁻²)	6657	2.9±0.6	0.7±0.3	0.8±0.2	0.7±0.2	0.14±0.03
	7230	2.0±0.5	1.5±0.4	0.2±0.1	0.4±0.1	0.25±0.03
	comb.	2.4±0.4	1.4±0.2	0.5±0.1	0.6±0.1	0.20±0.02

Note. — The regions are shown in Fig. 3. The errors represent statistical uncertainties at the 68% confidence level.

Table 3: Fits to the spectrum of B1929 for the *Chandra* and *XMM-Newton* observations.

Model	N_{H} 10^{21} cm^{-2}	Γ	PL Norm. $10^{-5} \text{ cm}^{-2} \text{ s}^{-1} \text{ keV}^{-1}$	kT keV	Radius ^a m	$\chi^2_{\nu}/\text{d.o.f}$	Absorbed Flux $10^{-13} \text{ ergs cm}^{-2} \text{ s}^{-1}$	Luminosity $10^{30} \text{ ergs s}^{-1}$
Chandra:								
PL	$2.45^{+0.52}_{-0.48}$	$2.94^{+0.25}_{-0.22}$	$7.99^{+1.76}_{-1.17}$	0.91/71	$1.37^{+0.14}_{-0.27}$	$6.26^{+2.66}_{-0.93}$
PL+BB	$0.49^{+0.93}_{-0.49}$	$1.82^{+1.04}_{-0.56}$	$1.91^{+3.86}_{-1.33}$	$0.29^{+0.05}_{-0.06}$	$33.8^{+46.3}_{-6.3}$	0.88/69	$1.52^{+0.23}_{-0.37}$	$4.66^{+0.86}_{-1.12}$
XMM-Newton:								
PL	$2.22^{+0.37}_{-0.30}$	$2.99^{+0.20}_{-0.15}$	$8.96^{+1.32}_{-0.96}$	0.97/190	$1.59^{+0.12}_{-0.25}$	$7.08^{+2.18}_{-0.84}$
PL+BB	$0.05^{+0.11}_{-0.05}$	$1.63^{+0.86}_{-0.29}$	$1.43^{+3.73}_{-0.42}$	$0.30^{+0.02}_{-0.05}$	$34.9^{+11.0}_{-4.9}$	0.94/188	$1.82^{+0.13}_{-0.26}$	$2.87^{+0.19}_{-0.39}$
combined:								
PL	$2.23^{+0.27}_{-0.27}$	$2.95^{+0.14}_{-0.13}$	$8.43^{+0.91}_{-0.79}$	1.03/264	$1.51^{+0.12}_{-0.24}$	$6.62^{+1.98}_{-0.82}$
PL+BB	$0.17^{+0.23}_{-0.17}$	$1.73^{+0.46}_{-0.66}$	$1.64^{+1.75}_{-0.28}$	$0.30^{+0.02}_{-0.03}$	$33.1^{+5.9}_{-4.6}$	0.98/262	$1.75^{+0.11}_{-0.22}$	$2.84^{+0.15}_{-0.22}$

Note. — The observed flux and unabsorbed luminosity, $L_X = 4\pi d^2 F_X^{\text{unabs}}$, are calculated for the 0.3–8 keV energy band for *Chandra*, and 0.3–10 keV for *XMM-Newton* and combined data. The listed uncertainties are at a 90% confidence level determined for 2 interesting parameters.

^aRadius of equivalent sphere for the BB component (see § 3.2).